

Local Operator Entanglement in Spin Chains

Eric Mascot¹, Masahiro Nozaki^{2,3}, and Masaki Tezuka⁴

¹ Department of Physics, University of Illinois at Chicago, Chicago, IL 60607, USA

² iTHEMS Program, RIKEN, Wako, Saitama 351-0198, Japan

³ Kavli Institute for Theoretical Sciences, and CAS Center for Excellence in Topological Quantum Computation, University of Chinese Academy of Sciences Beijing, 100190, China

⁴ Department of Physics, Kyoto University, Kyoto 606-8502, Japan

Abstract

We study the time evolution of bi- and tripartite operator mutual information of the time-evolution operator and Pauli's spin operators in the one-dimensional Ising model with magnetic field and the disordered Heisenberg model. In the Ising model, the early-time evolution qualitatively follows an effective light cone picture, and the late-time value is well described by Page's value for a random pure state. In the Heisenberg model with strong disorder, we find many-body localization prevents the information from propagating and being delocalized. We also find an effective Ising Hamiltonian describes the time evolution of bi- and tripartite operator mutual information for the Heisenberg model in the large disorder regime.

Contents

1	Introduction and summary	2
2	Preliminary	5
2.1	Information scrambling and operator spreading	5
2.2	Many-body localization (MBL)	8
2.3	Operator entanglement and its quantum measures	10
2.3.1	Definition of operator entanglement	10
2.3.2	Quantum measures	13

3	Time evolution of the BOMI and TOMI in spin chain	16
3.1	Early-time evolution	18
3.2	Late-time evolution	25
4	Time evolution of BOMI and TOMI in a disordered spin chain	28
4.1	Effective theory in the strong disordered phase.	32
5	Discussions and Future directions	35

1 Introduction and summary

Introduction

Thermalization is one of the frontier research topics in theoretical and experimental physics, in which entanglement of state plays an important role [1, 2, 3]. In closed quantum systems, the unitarity of the time evolution operator prevents a pure state from becoming a thermal state. However, in many cases, after an adequate amount of time, observables in a subsystem are well-approximated by those for a thermal state, known as thermalization. Though the thermal state does not depend on the entanglement structure of an initial state, thermalization *does* depend on the initial state and the details of its dynamics. Here, the entanglement structure refers to the way subsystems are entangled with each other. The reduced density matrix for a subsystem is given by a mixed state. If time evolution washes out the dependence of a mixed state on the details of the initial state, the reduced density matrix becomes the reduced thermal state. An effective temperature of the thermal state is given by the energy scale of the initial state. Even in anti-de Sitter/conformal field theory (AdS/CFT) correspondence [4], quantum entanglement sheds light on the mechanism behind the correspondence [5, 6].

To better understand thermalization, authors in [7, 8, 9, 10] studied the entanglement entropy in a quantum quench of conformal field theories. The entanglement entropy is the Von Neumann entropy of the reduced density matrix. A reduced density matrix becomes

approximately equal to the thermal state after enough time passes for the dynamics to wash out the information about the initial state.

The authors in [7] studied the time evolution of entanglement entropy for a subsystem of width l in two-dimensional (2D) CFTs. A given initial state depends on an initial energy scale, $1/\beta$. The time evolution of entanglement entropy after a quench follows the relativistic propagation of quasiparticles that are created by the quench. An entangled pair of particles is created on each site. Thereafter, one of the particles moves leftward at the speed of light, while the other moves rightward. When only one of these two particles remains in the subsystem, the entanglement entropy increases, owing to the entangled pair. For the early-time window, $\beta \ll t < \frac{l}{2}$, the entanglement entropy is a linear function of t , but when $\frac{l}{2} < t$, it is proportional to l . Thus, this volume law of entanglement entropy indicates the subsystem has thermalized.

The authors in [11, 12] found the time evolution of mutual information and entanglement entropy for two disjoint intervals in holographic CFT, a CFT that has a gravity dual, does not follow the quasiparticle interpretation. The early-time evolution follows the relativistic propagation of quasiparticles, but the late-time evolution does not. The authors in [13] found holographic tripartite mutual information, a linear combination of holographic mutual information, must be non-positive. These articles indicate the *multipartite entanglement* in CFTs depends on the details of the theories, such as operator contents. We think the multipartite entanglement sheds light on the details of thermalization. In [14, 15, 16, 17, 18, 19, 20, 21, 22, 23, 24], it was found that the operator entanglement, the entanglement of state dual to the operator, elegantly captures the details of dynamics in non-equilibrium processes. The operator entanglement of the time-evolution operator has the strong ability to show the quantum information in the initial subsystem is delocalized in the late-time regime, so that local observers are not able to obtain it. Therefore, we study the non-equilibrium phenomena, many-body localization (MBL) and operator spreading, using operator entanglement. These phenomena are the frontier topics in non-equilibrium physics.

Summary

We investigate the time evolution of bi- and tripartite operator mutual information of the time-evolution operator and Pauli's spin operators for three configurations, the fully-overlapping, partially-overlapping, and disjoint configurations, (See Figure 2) in a spin chain with strong scrambling ability and a disordered spin chain.

We divide the input (original) Hilbert space into A and \bar{A} , and divide the output (scattered) Hilbert space into B and \bar{B} . In the fully- or partially-overlapping configurations, A is initially in B . In the disjoint configuration, A is out of B . We summarize the results here.

Spin Chain with Strong Scrambling Ability

We consider a 1D Ising model with transverse and longitudinal field for its strong scrambling ability. We find that the time-evolution of bi- and tripartite operator mutual information is described by two effective descriptions, an effective light cone and Page curve.

Early time evolution: We find the early-time evolution of bi- and tripartite operator mutual information depends on the various operators and boundary conditions, and is described qualitatively by an effective light cone picture. In this picture, while sections of A , \bar{A} , B and \bar{B} are partially inside the light cone, the bipartite mutual information decreases. In the disjoint configuration, since the initial value of bipartite operator mutual information is small, the bipartite operator mutual information does not vary much, even after sections of A , \bar{A} , B and \bar{B} enter the light cone.

Late time evolution: We find the late-time evolution of bi- and tripartite mutual information is independent of various operators and boundary conditions, and the late time value is described by Page's value for the average entropy [25, 26], which we call the Page curve. Here, L denotes the size of input (original) and output (scattered) Hilbert spaces, and l is the size of the subsystem which we consider. In this picture, for $l < L$, operator entanglement entropy for this subsystem is a linearly-increasing function of l , and for $l > L$, the entropy is a linearly-decreasing function of l .

Disordered Spin Chain

We consider a 1D Heisenberg model with uniform disorder to study the many-body localization phase. We find parallels to the simpler Ising chain for the weak and strong disorder regimes.

Weak disorder: The spin chain with weak disorder is in the chaotic phase. Therefore, the late-time values of bi- and tripartite operator mutual information is well-described by the Page curve.

Strong disorder: If the magnitude of disorder is large, due to the many-body localization effect, the late-time value of bi-partite operator entanglement entropy in the fully- and partially overlapping configurations increases with disorder, and decreases in the disjoint configuration. If the disorder is large enough, due to local interactions, the time evolution of bi- and tripartite operator mutual information oscillates as a function of time. This oscillation is well-described by an effective Hamiltonian.

The authors in [24] have studied the late-time dynamics of many body localized systems by using operator mutual information and other quantities such as OTOC. Our results are consistent with theirs and we extend their results on operator mutual information to early-time dynamics.

2 Preliminary

In this section, we first describe the concepts of information scrambling and operator spreading. Second, we review many-body localization, which is an interesting dynamical phenomenon far from chaotic dynamics. Finally, we introduce operator entanglement and bipartite and tripartite operator mutual information as quantum measures for operator entanglement.

2.1 Information scrambling and operator spreading

Let us briefly review information scrambling and operator spreading.

Information scrambling

Information scrambling occurs in dynamical processes where the subsystem thermalizes after an adequate amount of time. To explain information scrambling, we first review thermalization of subsystems. Consider the initial state

$$|\Psi\rangle = \sum_{E_\alpha < 1/\epsilon} C_\alpha |\alpha\rangle \approx \sum_{\alpha} e^{-\epsilon H} C_\alpha |\alpha\rangle, \quad (2.1)$$

where $|\alpha\rangle$ is an eigenstate of Hamiltonian, $H|\alpha\rangle = E_\alpha|\alpha\rangle$ and $E_\alpha \geq 0$. We approximate the cutoff $\sum_{\alpha}^{1/\epsilon}$ by the weight $\sum_{\alpha} e^{-\epsilon H}$. This initial state is characterized by an energy scale, $1/\epsilon$. The low-energy modes $|E_\alpha \leq 1/\epsilon\rangle$ dominantly contribute to the initial state.

Following the time evolution $U(t)$, the reduced density matrix for a subsystem \mathcal{V} is given by

$$\rho_{\mathcal{V}}(t) = \text{Tr}_{\bar{\mathcal{V}}} [U(t) |\Psi\rangle \langle \Psi| U^\dagger(t)], \quad (2.2)$$

where we divide the total Hilbert space into \mathcal{V} and $\bar{\mathcal{V}}$. The reduced density matrix $\rho_{\mathcal{V}}(t)$ depends not only the initial state, but also on the details of time-evolution operator $U(t)$. If $\rho_{\mathcal{V}}(t)$ is well-approximated by a reduced thermal density with an effective inverse temperature $\beta_{\text{eff}} \approx \epsilon$ after some time,

$$\rho_{\mathcal{V}}(t) \xrightarrow{t \rightarrow \infty} \text{Tr}_{\bar{\mathcal{V}}} e^{-\epsilon H}, \quad (2.3)$$

then the subsystem \mathcal{V} has thermalized. In other words, if the observables in \mathcal{V} such as the one-point function and the distance between states [27, 28, 29] is approximately given by

$$\lim_{t \rightarrow \infty} \langle \Psi| U^\dagger(t) V(x) U(t) |\Psi\rangle \approx \text{Tr} (e^{-\epsilon H} V(x)) \quad (2.4)$$

$$\lim_{t \rightarrow \infty} \text{Tr}_{\mathcal{V}} (\rho_{\mathcal{V}}(t) \text{Tr}_{\bar{\mathcal{V}}} e^{-\epsilon H}) \approx \sqrt{\text{Tr}_{\mathcal{V}} (\text{Tr}_{\bar{\mathcal{V}}} e^{-\epsilon H})^2 \text{Tr}_{\mathcal{V}} (\rho_{\mathcal{V}}(t))^2}, \quad (2.5)$$

then thermalization of \mathcal{V} occurs. If the approximation in (2.3) works well, the late-time reduced density matrix depends only on the initial energy $1/\epsilon$ and not on the entanglement structure of its initial state. Information scrambling is the phenomenon where the late-time reduced density matrices for any subsystem is independent of the structure of its initial

state, and instead depends on $1/\epsilon$. If this phenomenon occurs, dynamics has the strongest scrambling ability.

Operator spreading

One of interesting, dynamical phenomena is operator spreading [14, 30, 31, 32]. A local operator in the Heisenberg picture $\mathcal{O}(x, t)$ is given by

$$\begin{aligned}\mathcal{O}(x, t) &= e^{itH}\mathcal{O}(x)e^{-iHt} \\ &= \mathcal{O}(x) + (it)[H, \mathcal{O}(x)] + \frac{(it)^2}{2!}[H, [H, \mathcal{O}(x)]] + \dots, \end{aligned} \quad (2.6)$$

where we used the Baker-Campbell-Hausdorff formula. If t is small, $\mathcal{O}(x, t)$ is approximately given by a simple operator $\mathcal{O}(x)$. As time proceeds, the larger the contributions of terms with higher powers of t become. Thus, a local operator in the Heisenberg picture $\mathcal{O}(x, t)$ becomes more complicated over time.

Consider a probe $\mathcal{Q}(y)$, a local operator far from the position of \mathcal{O} , to measure how much $\mathcal{O}(x, -t)$ spreads. If t is small, this probe is causally unrelated to $\mathcal{O}(x, -t)$,

$$[\mathcal{Q}(y), \mathcal{O}(x, -t)] = 0. \quad (2.7)$$

If t is large, this probe is causally related to $\mathcal{O}(x, -t)$,

$$[\mathcal{Q}(y), \mathcal{O}(x, -t)] \neq 0. \quad (2.8)$$

This is *operator spreading*. The expectation value of the square of the commutator $\langle [\mathcal{Q}(y), \mathcal{O}(x, -t)]^2 \rangle$ measures how much $\mathcal{O}(x, -t)$ spreads and how complicated it becomes. If the Hamiltonian has the strongest scrambling ability, the expectation $\langle [\mathcal{Q}(y), \mathcal{O}(x, -t)]^2 \rangle$ in the late-time region is exponentially large,

$$\langle [\mathcal{Q}(y), \mathcal{O}(x, -t)]^2 \rangle \gg 1 \quad (2.9)$$

where the exponential increase of $\langle [\mathcal{Q}(y), \mathcal{O}(x, -t)]^2 \rangle$ implies that the out of time-ordered correlator exponentially increases.

2.2 Many-body localization (MBL)

Many-body localization is a counterexample to thermalization, which says the structure of quantum entanglement is almost preserved under time-evolution. Therefore, we expect quantum information to be preserved locally.

The localization of energy eigenstates up to finite energy density in interacting quantum systems, termed many-body localization, has received wide attention for more than a decade. See [33, 34, 35] for recent review articles.

In the non-interacting case the single-particle orbitals can localize due to randomness [36]. It was initially not clear whether localization persists in the presence of interactions. In the tight-binding picture, a particle localizing around a lower energy lattice site would repel other particles if the interaction between the particles is repulsive, as would be expected for electrons with Coulomb interactions. Then the effect of the interaction would be to weaken the randomness in the site energy. In later studies, the possibility of localization was first discussed for the many-body ground state [37, 38, 39], and then to finite-temperature cases [40, 41, 42]. Interacting systems staying insulating at finite temperatures are said to be many-body localized.

An MBL state can escape thermalization when placed in a non-equilibrium initial state. Integrable systems also do not generally thermalize, but the integrability sensitively depends on the choice of parameters and thermalization would happen once the integrability is broken, unless MBL is established. MBL phases are robust against weak perturbations since all the energy eigenstates are localized up to a finite energy density. In systems with a set of random parameters (e.g. hoppings, site energies, or on-site interactions) drawn from some probability distributions, any physical quantities would be probabilistically determined. However, once the constants controlling these distributions satisfy certain conditions, the probability that the MBL behavior is not observed is exponentially small, then the system controlled by these constants can be said to be in the MBL phase.

Note that systems that exhibit MBL without randomness in the Hamiltonian have been

proposed [43]. Also, note that quasiperiodic systems, whose non-uniform feature is determined by a few parameters as opposed to lacking long-range correlation, can be many-body localized. Even in these cases, we can generally expect the many-body localized phase to be robust against noise.

Hamiltonians exhibiting the MBL phase provide counterexamples to the most general, or naive, form of the eigenstate thermalization hypothesis (ETH) [44, 45]. ETH states that for an isolated quantum mechanical many-body system, for any initial state given as a linear combination of eigenstates close in energy, the expectation value of an operator should “thermalize”, that is, relax to a value close to the one expected for the microcanonical ensemble determined by the energy range and will only show small fluctuations at later times.

A kind of emergent integrability exists in the many-body localized systems, as there are exponentially many quasi-local integrables of motion, often abbreviated as LIOMs. Correspondingly, the energy spectrum does not show the random matrix universality as expected in a quantum chaotic system [46] and become uncorrelated.

The time evolution of entanglement entropy from an uncorrelated state, which would be linear in non-interacting systems or general non-integrable systems without localization [47], becomes logarithmic in time for a many-body localized system [48, 49, 50, 51]. In a many-body localized eigenstate the entanglement entropy for a subsystem exhibits area law dependence on the surface area rather than volume laws that is expected for a thermal reduced density matrix for the subsystem obeying ETH [52].

Experimentally, MBL has been observed in ultracold atoms [53, 54, 55, 56] and ions [57] trapped in low dimensions. In [53], the atoms were prepared in a highly non-equilibrium density-wave state, in which most of the particle population is on every second lattice site in a one-dimensional lattice. Then, the system was allowed to evolve under the given Hamiltonian and the imbalance between the even and odd sites was measured. In the presence of the on-site interaction, the imbalance remained finite when the quasiperiodic potential was strong

enough.

2.3 Operator entanglement and its quantum measures

In this section, we describe of operator entanglement and the quantum measures which we consider in this paper, bipartite operator mutual information (BOMI) and tripartite operator mutual information (TOMI).

2.3.1 Definition of operator entanglement

Operator entanglement is defined as the entanglement structure of the dual state, which is the state given by a state-channel map:

$$\mathcal{W} = \sum_i \mathcal{W}_i |i\rangle \langle i| \xrightarrow{\text{state-channel map}} |W\rangle = \mathcal{N} \sum_i \mathcal{W}_i |i\rangle |i^*\rangle, \quad (2.10)$$

where \mathcal{W} is an operator, $|i^*\rangle$ is a *CPT* conjugate of $|i\rangle$, and \mathcal{N} is a normalization factor. The dual state lives in the Hilbert space whose dimension is the square of the dimension of the original Hilbert space:

$$\mathcal{H}_{\mathcal{W}} \xrightarrow{\text{state-channel map}} \mathcal{H}_{|W\rangle} = \mathcal{H}_{\mathcal{W}} \otimes \mathcal{H}_{\mathcal{W}}, \quad (2.11)$$

where $\mathcal{H}_{\mathcal{W}}$ is the Hilbert space where the operator acts, and $\mathcal{H}_{|W\rangle}$ is the space where the dual state lives.

In this paper, we consider the operator entanglement of the following operators.

Unitary operator

Time evolution changes the local entanglement structure of an initial state. The quantum correlation between a subsystem A of an initial state and subsystem B of the time-evolved state should show how the time evolution changes the local structure of an initial state. The information about the local structure propagates (and/or is delocalized) as the structure changes. In this paper, we define operator entanglement measurements of the unitary time-evolution operator, and study *the spreading and delocalization of quantum information* by

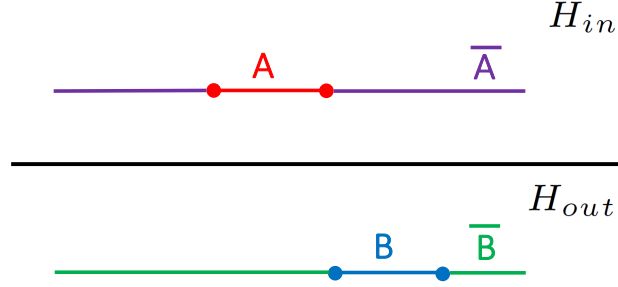


Figure 1: Input (A) and output (B) subsystems in the doubled Hilbert space $H_{\text{in}} \otimes H_{\text{out}}$. We compute the BOMI and TOMI for the configurations corresponding to Figure 2.

using the measures for operator entanglement defined in Section 2.3.2. The unitary channel for the time-evolution operator $U(t)$, represented in the eigenbasis of the Hamiltonian, is

$$U(t) = e^{-iHt} = \sum_a^N e^{-itE_a} |a\rangle \langle a|, \quad (2.12)$$

where the Hamiltonian is a time-independent operator, $|a\rangle$ is an eigenstate, and N is the number of states.

The dual state to (2.12) can be defined by the state-channel map $f[U(t)]$,

$$\begin{aligned} f[U(t)] = |U(t)\rangle &= \frac{1}{\sqrt{N}} \sum_a^N e^{-itE_a} |a\rangle |a\rangle = \frac{1}{\sqrt{N}} \sum_a^N e^{-itE_a} |a\rangle |a\rangle \\ &= \frac{1}{\sqrt{N}} \sum_a^N e^{-\frac{it}{2}(H_{\text{in}}+H_{\text{out}})} |a\rangle_{\text{in}} |a\rangle_{\text{out}}, \end{aligned} \quad (2.13)$$

where we take $|a\rangle$ to be a real function because $|a\rangle$ is an eigenstate of H . The states, $|\cdot\rangle_{\text{in}}$ and $|\cdot\rangle_{\text{out}}$, live in the Hilbert spaces, \mathcal{H}_{in} and \mathcal{H}_{out} . Thus, the state defined in (2.13) lives in $\mathcal{H} = \mathcal{H}_{\text{in}} \otimes \mathcal{H}_{\text{out}}$. Its density matrix is given by

$$\rho = |U(t)\rangle \langle U(t)| = \frac{1}{N} \sum_{a,b=1}^N e^{-it(E_a-E_b)} |a\rangle_{\text{in}} \langle b|_{\text{in}} \otimes |a\rangle_{\text{out}} \langle b|_{\text{out}}. \quad (2.14)$$

We divide the input Hilbert space \mathcal{H}_{in} into \mathcal{H}_A and $\mathcal{H}_{\bar{A}}$ and the output Hilbert space \mathcal{H}_{out} into \mathcal{H}_B and $\mathcal{H}_{\bar{B}}$ as in Figure 1. The input and output states in the spacetime language are

given by

$$\begin{aligned} |a\rangle_{\text{in}} &= \sum_{iI} C_{iI}^a |i\rangle_A |I\rangle_{\bar{A}}, |b\rangle_{\text{in}} = \sum_{jJ} C_{jJ}^b |j\rangle_A |J\rangle_{\bar{A}}, \\ |a\rangle_{\text{out}} &= \sum_{\alpha A} D_{\alpha A}^a |\alpha\rangle_B |\mathcal{A}\rangle_{\bar{B}}, |b\rangle_{\text{out}} = \sum_{\beta B} D_{\beta B}^b |\beta\rangle_B |\mathcal{B}\rangle_{\bar{B}}, \end{aligned} \quad (2.15)$$

where $|x\rangle_X$ are orthogonal vectors in \mathcal{H}_X and $X = A, \bar{A}, B, \bar{B}$. Thus, the density matrix in the spacetime language is given by

$$\rho = \frac{1}{N} \sum_{a,b,i,j,I,J,\alpha,\beta,A,B} e^{-it(E_a - E_b)} C_{iI}^a C_{jJ}^{b*} D_{\alpha A}^a D_{\beta B}^{b*} |i\rangle \langle j|_A \otimes |I\rangle \langle J|_{\bar{A}} \otimes |\alpha\rangle \langle \beta|_B \otimes |\mathcal{A}\rangle \langle \mathcal{B}|_{\bar{B}}. \quad (2.16)$$

Next, we consider a reduced density matrix for $A \cup B$ as an example. The matrix ρ_{AUB} is given by limiting the sum in the above to $I = J$ and $\mathcal{A} = \mathcal{B}$,

$$\begin{aligned} \rho_{AUB} &= \text{Tr}_{\overline{AUB}} \rho = \frac{1}{N} \sum_{a,b,i,j,J,\alpha,\beta,B} e^{-it(E_a - E_b)} C_{iJ}^a C_{jJ}^{b*} D_{\alpha B}^a D_{\beta B}^{b*} |i\rangle \langle j|_A \otimes |\alpha\rangle \langle \beta|_B \\ &= \sum_{a,b,i,j,J,\alpha,\beta,B} e^{-it(E_a - E_b)} \mathcal{M}_{ij}^{ab} \mathcal{N}_{\alpha\beta}^{ab} |i\rangle \langle j|_A \otimes |\alpha\rangle \langle \beta|_B, \end{aligned} \quad (2.17)$$

where $\mathcal{M}_{ij}^{ab} = \sum_J C_{iJ}^a C_{jJ}^{b*}$ and $\mathcal{N}_{\alpha\beta}^{ab} = \sum_B D_{\alpha B}^a D_{\beta B}^{b*}$. Operator entanglement entropy (OEE) for ρ_{AUB} is defined as a free energy of the reduced density matrix

$$S_{AUB} = -\text{Tr}_{AUB} \rho_{AUB} \log \rho_{AUB} = - \sum_{\lambda_{AUB}} \lambda_{AUB} \log \lambda_{AUB} \quad (2.18)$$

where λ_{AUB} are the eigenvalues of ρ_{AUB} .

By computing the mutual information (defined in Section 2.3.2) of the unitary time-evolution operator, we study the correlation between a subsystem of the initial state and a subsystem of the output state in which we measure local observables.

Local operator

A local perturbation, a perturbation due to a local operator, spreads under the time evolution as in Section 2.1, so that the entanglement structure of the scattered state, the state which is acted with the local operator, should differ from the original state. By measuring the correlation between the subsystem A of the original state and B of the scattered state, we

should find where information about the entanglement structure in A propagates and how much the operator delocalizes information. Let us define the local operator entanglement as the quantum entanglement of local operator $\mathcal{O}(x, t)$ as follows.

A local operator in Heisenberg picture $\mathcal{O}(x, t)$ is defined as

$$\mathcal{O}(x, t) = e^{iHt}\mathcal{O}(x)e^{-iHt}, \quad (2.19)$$

where we assume that the Hamiltonian is time-independent. We define the state dual to (2.19) by the channel-state map:

$$|\mathcal{O}(x, t)\rangle = \mathcal{N} \sum_{ab} e^{itE_a} \langle a|_{\text{out}} \mathcal{O}(x) |b\rangle_{\text{in}} e^{-itE_b} |a\rangle_{\text{out}} |b\rangle_{\text{in}} = \mathcal{N} \sum_{ab} \langle a|_{\text{out}} \mathcal{O}(x, t) |b\rangle_{\text{in}} |a\rangle_{\text{out}} |b\rangle_{\text{in}}, \quad (2.20)$$

where the states $|\cdot\rangle_{\text{in}}$ and $|\cdot\rangle_{\text{out}}$ are the eigenstates of the time-independent Hamiltonian, and the normalization factor \mathcal{N} is given by

$$\mathcal{N} = Z^{-\frac{1}{2}}, \quad Z = \text{Tr}(\mathcal{O}^\dagger(x)\mathcal{O}(x)). \quad (2.21)$$

The entanglement structure of the state in (2.20) strongly depends on the Heisenberg operator. The definition in (2.20) shows that the local operator dual state is less than maximally-entangled unless $\mathcal{O}(x, t)$ is the identity operator. By computing the mutual information (defined in Section 2.3.2) of local operators, we study the correlation between the subsystem A of the original state and the one B of the scattered state.

2.3.2 Quantum measures

Operator mutual information measures non-local correlation between subsystems. As mentioned in the previous sections, we investigate the time evolution of the operator mutual information in various configurations in order to find how operator spreading occurs under time-evolution for a system with strong scrambling ability. We also study the operator mutual information in a system which has a many-body localized phase.

Bipartite operator mutual information (BOMI)

Bipartite operator mutual information (BOMI) is defined as the linear combination of OEE

$$I_{A,B} = S_A + S_B - S_{A \cup B}, \quad (2.22)$$

where S_A and S_B are OEEs for the input (original) subsystem A and the output (scattered) subsystem B . The last term in the right-hand side in (2.22) is OEE for $A \cup B$. The input and output subsystems are defined as the subsystems of $H_{\text{in}} \otimes H_{\text{out}}$ where the dual state to $U(t)$ lives, while the original and scattered subsystems are defined as the subsystems of $H_{\text{original}} \otimes H_{\text{scattered}}$ where the state dual to $\mathcal{O}(t, x)$ lives. The BOMI measures the correlation between the input (original) and output (scattered) subsystems. If $I_{A,B}$ vanishes, there are no correlations between A and B , which means that the reduced density matrices of the subsystems are unrelated to each other.

Tripartite operator mutual information (TOMI)

Tripartite operator mutual information (TOMI) is defined as a linear combination of the BOMI as follows. We divide the output or scattered space into the subsystems B and \bar{B} , and also divide the input or original space into A and \bar{A} . The TOMI which we consider is given by

$$I_{A,B,\bar{B}} = I_{A,B} + I_{A,\bar{B}} - I_{A,B \cup \bar{B}}, \quad (2.23)$$

where the first two terms in the right-hand side of (2.23) measures the correlation between the input (original) subsystem A and the output (scattered) subsystems, and the last term measures the correlation between A and the whole output (scattered) space. As in [13, 14, 21, 22, 20], the TOMI in (2.23) measures how much information regarding A is delocalized over time.

Configurations

As shown in Figure 2, we study the time evolution of the operator mutual information in three configurations: (a)full overlap, (b)partial overlap, and (c)disjoint configurations. In

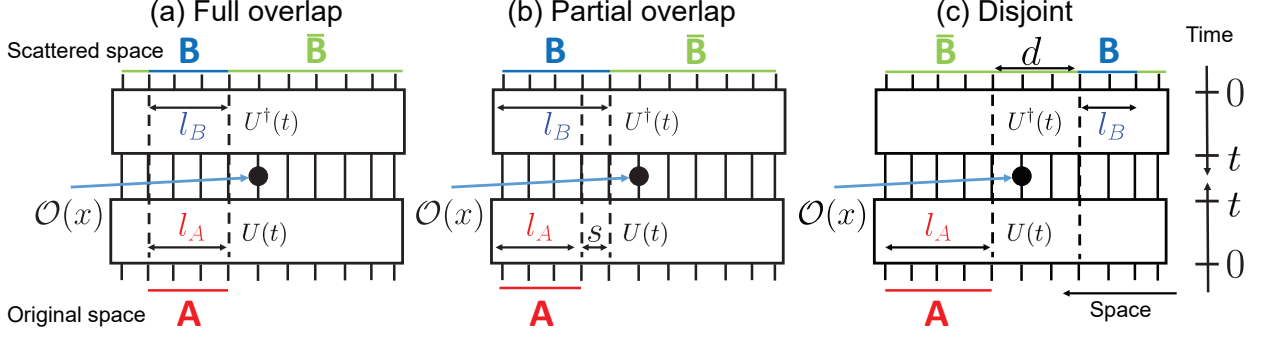


Figure 2: Schematic of the three configurations: (a) full overlap, (b) partial overlap, and (c) disjoint. Full overlap: The size of A and B are equal, $l_A = l_B$, and are aligned. Partial overlap: The size of B is greater than A by s , $l_A + s = l_B$, and are aligned on the left. Disjoint: The distance between the right boundary of A and the left boundary of B is d .

the full overlap configuration, the size of A and B are equal, $l_A = l_B$, and the edges of each subsystem are aligned. In the partial overlap configuration, the size of B is larger than that of A by s , $l_B = l_A + s$. The left edge of subsystems A and B are aligned. In the disjoint configuration, the subsystems A and B do not have any overlapping regions and the distance between the right edge of A and left edge of B is d .

- **Unitary operator in full overlap configuration:** The time evolution of $I_{A,B}$ shows how much information about the local entanglement structure of the initial state remains under time evolution, while that of $I_{A,B,\bar{B}}$ shows how much information with respect to A is non-localized through the time evolution.

Local operator in the full overlap configuration: The scrambling ability of the unitary time evolution makes the local operator spread, so that the entanglement structure of the state in the output (scattered) Hilbert space differs from that in the input (original) Hilbert space. In order to study how different the local entanglement structure of B is from A , we study the time evolution of $I_{A,B}$. The time evolution of $I_{A,B,\bar{B}}$ shows how the operator spreading delocalizes the information in reference to A .

- **Unitary operator in the partial overlap configuration:** Figure 2(b) is the configuration that shows how the dynamics spreads the information concerning A across B ,

which is larger than A , by tracking the time evolution of $I_{A,B}$. The time evolution of $I_{A,B,\bar{B}}$ indicates how much data regarding the local entanglement structure delocalizes under the time evolution.

Local operator in the partial overlap configuration: The spreading of information with respect to A should proceed according to the spreading of the local operator. We study the spreading of information in reference to A by measuring the time evolution of $I_{A,B}$. The time evolution of $I_{A,B,\bar{B}}$ indicates how the spreading of operator makes information about A delocalizes.

- **Unitary operator in the disjoint configuration:** By tracking the time evolution of $I(A, B)$ for disjoint configurations (Figure 2(c)), we study how much information is sent from A to a disjoint interval B under time evolution.

Local operator in the disjoint configuration: The time evolution $I_{A,B}$ of a local operator for the two disjoint intervals indicates how much the operator has spread from A to B .

3 Time evolution of the BOMI and TOMI in spin chain

We study the dynamics of the spin chain,

$$H = \sum_{i=1}^L [\sigma_z^{(i)} \sigma_z^{(i+1)} + h_x \sigma_x^{(i)} + h_z \sigma_z^{(i)}], \quad (3.1)$$

where L is the number of site of this system, and $\sigma_a^{(i)}$ are the Pauli spin operators on site i . For periodic boundary conditions, we define $\sigma_a^{(L+1)} = \sigma_a^{(1)}$, whereas for open boundary conditions, the term involving $\sigma_a^{(L+1)}$ is ignored. The dynamics of the Hamiltonian with $(h_x, h_z) = (-1.05, 0.5)$ is chaotic [29, 58].

The authors in [14] studied the time evolution of the BOMI and TOMI for the unitary operator $U(t)$, and in particular, studied the scrambling ability of the chaotic chain. In this paper, we study the scrambling ability of the chain in terms of local operators, and compare

the BOMI and TOMI of local operators to $U(t)$. We consider the time evolution for Pauli's operators in the Heisenberg picture $\sigma_a^{(i)}(t) = e^{iHt}\sigma_a^{(i)}e^{-iHt}$ for a spin chain with periodic and open boundary conditions.

We investigate the time evolution of the BOMI and TOMI in the integrable and chaotic phases. We briefly summarize the results:

1. **Integrable phase:** For integrable cases, we study both longitudinal, $(h_x, h_z) = (0, 2)$, and transverse, $(h_x, h_z) = (0.5, 0)$, magnetic fields [59].

In the longitudinal case, H and $\sigma_z^{(i)}$ commute. Therefore, the BOMI and TOMI of $\sigma_z^{(i)}$ are independent of time. The BOMI and TOMI of σ_x and σ_y are either constant or periodic functions in time, depending on the location of the operator and the boundary conditions. The BOMI and TOMI of $U(t)$ is always a periodic function in time but the amplitude depends on the boundary conditions.

The parameters $(h_x, h_z) = (0.5, 0)$ are also in the integrable phase. However, the BOMI and TOMI of all operators are neither constant nor periodic functions. Even the late-time evolution of the BOMI and TOMI depends on the operators and boundary conditions.

2. **Chaotic phase:** For the parameters $(h_x, h_z) = (-1.05, 0.5)$, the system is chaotic.
 - *Early-time evolution:* An effective light cone picture explained in section 3.1 qualitatively describes the early-time evolution of the BOMI and TOMI of the local operators for the full and partial overlap configurations. The value of the BOMI in the disjoint configuration is very small, which implies that little information spreads.
 - *Late-time evolution:* The late-time values for the full and partial overlap configurations are independent of the operators and boundary conditions, and become the same as the unitary operator. The Page curve, explained in 3.2, describes the

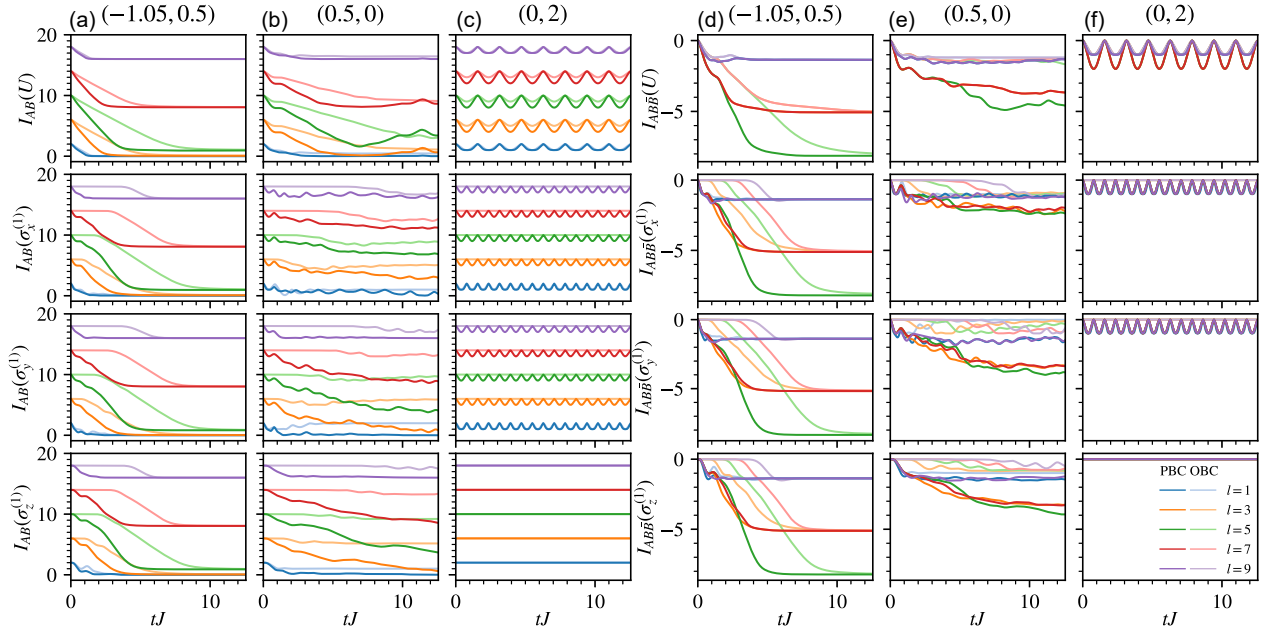


Figure 3: Time evolution of the (a-c) BOMI and (d-f) TOMI of the operators U , $\sigma_x^{(1)}$, $\sigma_y^{(1)}$, and $\sigma_z^{(1)}$ in the chaotic chain model for the fully overlapping configuration. The local operators are located at the left boundary of A and B and the size of A and B are equal, $l_A = l_B = l$. The magnetic field is $(h_x, h_z) = (-1.05, 0.5)$ for (a,d), $(h_x, h_z) = (0.5, 0)$ for (b,e), and $(h_x, h_z) = (0, 2)$ for (c,f). Dark lines correspond to periodic boundary conditions and light lines correspond to open boundary conditions. The total number of sites is $L = 10$.

late-time values of the BOMI for these configurations. The value of the BOMI in the disjoint configuration is very small since it was initially small.

In Figures 3, 4, and 5, we show the time evolution of the BOMI and TOMI for the full overlap, partial overlap, and disjoint configurations, respectively. In the following subsections, we explain the time evolution of the BOMI and TOMI in detail.

3.1 Early-time evolution

Let us explain the early-time evolution of the BOMI and TOMI for the three configurations in Figure 2. We divide the input (original) system of size L into A and \bar{A} of size l_A and $L - l_A$, and the output (scattered) system, also of size L , into B and \bar{B} of size l_B and $L - l_B$. We consider periodic boundary conditions (PBC) and open boundary conditions (OBC).

In Figure 3, we show the time evolution of the BOMI in panels (a,b,c) and TOMI in panels

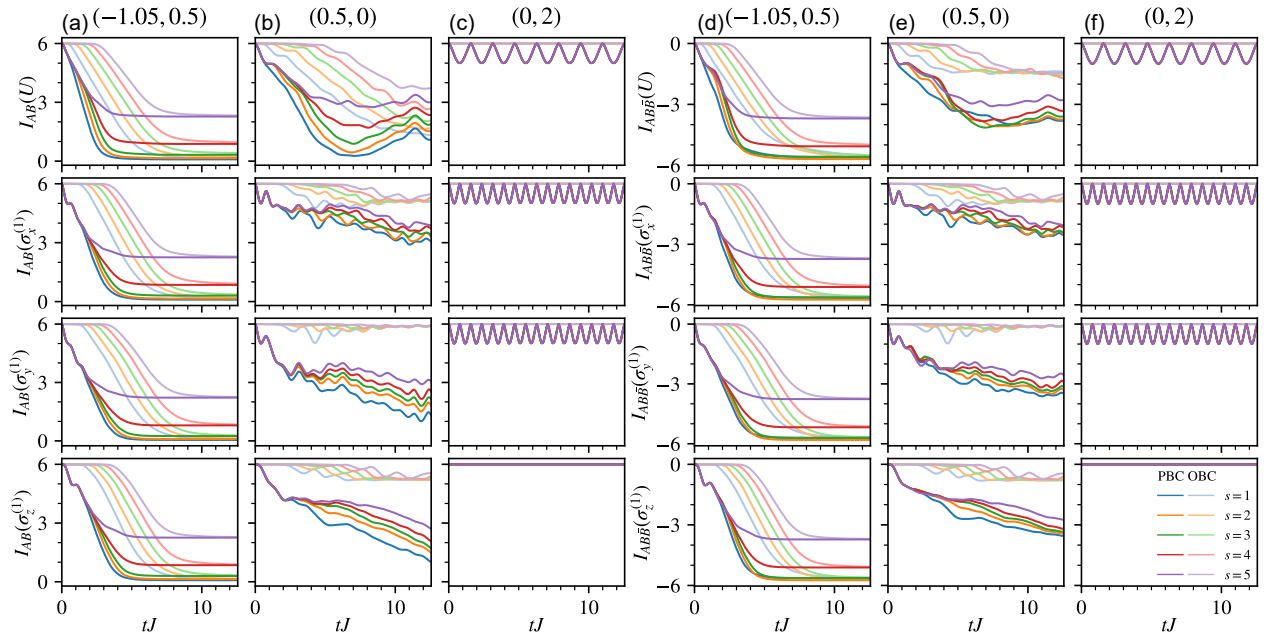


Figure 4: Time evolution of the (a-c) BOMI and (d-f) TOMI of the operators U , $\sigma_x^{(1)}$, $\sigma_y^{(1)}$, and $\sigma_z^{(1)}$ in the chaotic chain model for the partially overlapping configuration. The local operators are located at the left boundary of A and B and the size of B is greater than the size of A by s , $l_A + s = l_B$. The magnetic field is $(h_x, h_z) = (-1.05, 0.5)$ for (a,d), $(h_x, h_z) = (0.5, 0)$ for (b,e), and $(h_x, h_z) = (0, 2)$ for (c,f). Dark lines correspond to periodic boundary conditions and light lines correspond to open boundary conditions. The total number of sites is $L = 10$ and the number of sites in A is $l_A = 3$.

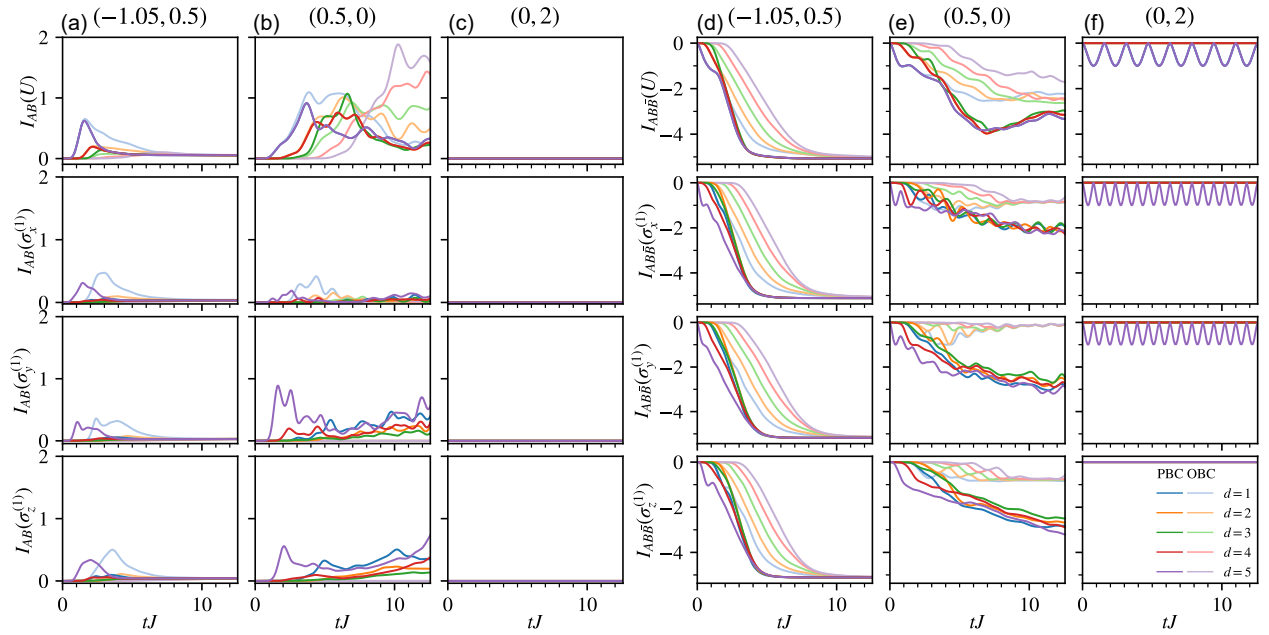


Figure 5: Time evolution of the (a-c) BOMI and (d-f) TOMI of the operators U , $\sigma_x^{(1)}$, $\sigma_y^{(1)}$, and $\sigma_z^{(1)}$ in the chaotic chain model for the disjoint configuration. The local operators are located at the left boundary of A and the left boundary of B is a distance d from the right boundary of A . The magnetic field is $(h_x, h_z) = (-1.05, 0.5)$ for (a,d), $(h_x, h_z) = (0.5, 0)$ for (b,e), and $(h_x, h_z) = (0, 2)$ for (c,f). Dark lines correspond to periodic boundary conditions and light lines correspond to open boundary conditions. The total number of sites is $L = 10$ and the number of sites in A and B are $l_A = l_B = 3$.

(d,e,f) for the full overlap configuration, as shown in Figure 2(a). The BOMI and TOMI are defined by (2.22) and (2.23). In this configuration, $l_A = l_B = l$. The local operators $\sigma_{a=x,y,z}^{(1)}$ are at the leftmost site of A and B . In the open spin chain, the local operator site is also the leftmost site of the system. In panels (a,b,c), the BOMI always starts at $2l$. In the chaotic phase in panel (a), the BOMI begins to decrease instantly, but the slope depends on the boundary conditions. This is explained by a light cone picture. The BOMI then settles on a stable value, described by the Page curve. Both the light cone and Page curve will be described in more detail in the next sections. The BOMI for the integrable phases are shown in panels (b,c). For longitudinal field, shown in (c), the BOMI for σ_z is always constant and the BOMI for U oscillates. For σ_x and σ_y , the BOMI oscillates for PBC and is constant for OBC except for $l = 1$ where it is constant. For transverse field, shown in (b), the dynamics has some scrambling ability and shows characteristics similar to (a), but also has some oscillatory behavior similar to (c). The TOMI always starts at zero. In the chaotic phase, shown in (d), the TOMI decreases and settles on a value depending on l . The late-time value is the same for l and $L - l$. For transverse field in (e), the TOMI shows unpredictable behavior, but is in general, more negative for PBC. For longitudinal field in (f), the TOMI shows consistent oscillatory behavior below zero or stays constant at zero.

In Figure 4, we show the time evolution of the BOMI and TOMI for the partial overlap configuration. In this configuration, the number of sites in B is larger than A by s . The size of B is equal to $l_B = l_A + s$. In Figure 4, we show the time evolution of $I_{A,B}$ and $I_{A,B,\bar{B}}$ for $l_A = 3$. The BOMI in the chaotic phase, shown in (a), decreases instantly for PBC but has a delay for OBC and this delay is later for larger s . The BOMI then settles on a value close to zero for $l_B < L/2$. In the integrable phase, the BOMI for transverse field, shown in (b), shows unpredictable behaviour, but is negative and decreases in general. The BOMI for longitudinal field in (c) shows the same behavior as the full overlap configuration in Figure 3(c). The TOMI in the partial overlap configuration is similar to the full overlap configuration. For the chaotic phase, however, we see that the decrease of the TOMI is delayed for OBC with

increasing delay for larger s .

In Figure 5, the BOMI and TOMI for the disjoint configuration is shown. In this figure, $l_A = l_B = l = 3$. the distance between the rightmost of A and the leftmost of B is d . The BOMI and TOMI for both chaotic and integrable phases start at zero. The BOMI in the chaotic phase in (a) shows a small bump at an early time and then returns close to zero. The BOMI in the integrable phase increases slightly for transverse field (b) and remains zero for longitudinal field (c). The TOMI for the disjoint configuration is similar to the full and partial overlap configurations.

As in [60], quantum revival occurs in a 2 dimensional free field theory on a compact manifold. Here, quantum revival refers to the BOMI returning to its initial value. The revival time is proportional to the system size, because the revival in the free field theory follows the relativistic propagation of quasi-particles. The BOMI for PBC in the chaotic phase does not return to the original one. Therefore, the revival does not occur for PBC in the chaotic phase.

Chaotic chain $(h_x, h_z) = (-1.05, 0.5)$

We find the time evolution of the BOMI and TOMI of local operators in the chaotic phase qualitatively follows an effective light cone picture. Let us explain the effective light cone picture, which well-describes the distinctive behaviors of the early-time BOMI and TOMI of Pauli's spin operators in the chaotic phase of (3.1). Consider a local operator in the Heisenberg picture $\mathcal{O}(x, t)$. As in Figure 6, we call the original (scattered) subspace in the light cone *original (scattered) interior*. The interior of effective light cone is the region where $\mathcal{O}(x, t)$ has influence: The local operator makes changes to the entanglement structure of the scattered subspace. The exterior of the light cone is approximately equal to a local identity. The size of the original and scattered subsystems inside of the light cone, l_i , depends on an effective velocity, v_{eff} , determined by the details of theory. When v_{eff} is a constant velocity,

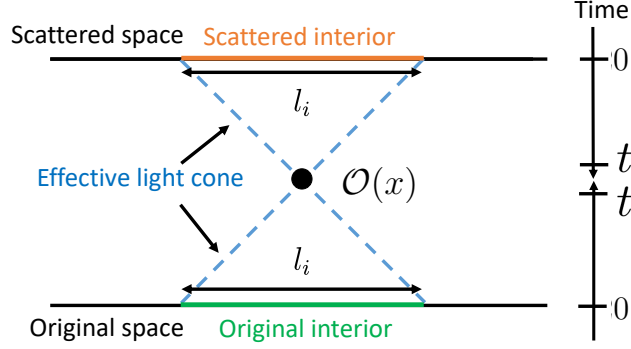


Figure 6: Schematic of the effective light cone for a local operator $\mathcal{O}(x, t)$. The interior of the light cone grows in time. Information in the interior of the light cone from the original space is communicated through the local operator to the interior of the light cone of the scattered space. The local operator is approximately identity in the exterior of the light cone.

l_i is determined by v_{eff} ,

$$l_i = 2v_{\text{eff}}t. \quad (3.2)$$

Here, we divide the original Hilbert space into A and \bar{A} , while we divide the scattered Hilbert space into B and \bar{B} . In this picture, if A_l and B_l (A_r and B_r) are in the light cone and A_r and B_r (A_l and B_l) are not as in (a) of Figure 7((b) of Figure 7), then BOMI and TOMI decreases. In the early time interval, as in panels (a) and (b) of Figure 7, A_l and B_l (A_r and B_r) are in the light cone and A_r and B_r (A_l and B_l) are not, so that $I_{A,B}$ decreases. After enough time, as in the panes (c) and (d) of Figure 7, A_l , B_l , A_r , and A_l are in the light cone, so that the slope of $I_{A,B}$ flattens. In Figure 8, we show the light cone picture effectively describes the time evolution of $I_{A,B}$. For the disjoint configuration, A is almost uncorrelated to B , initially. Then, $I_{A,B}$ becomes small compared to the other configurations, as seen in Figure 5. In 2 dimensional holographic CFTs, which are theories that have a gravity dual, the time evolution of operator BOMI and TOMI is well-described by a very simple explanation, the line tension picture[23].

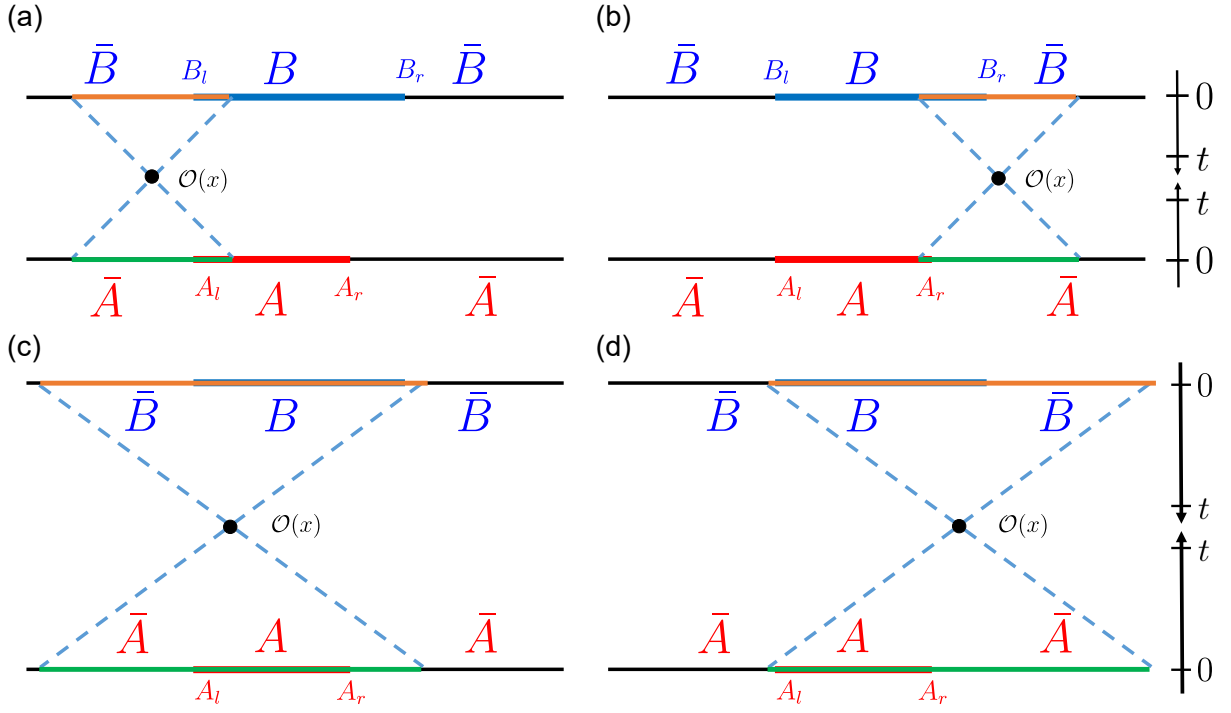


Figure 7: Schematic of the effective light cone in the partially overlapping configuration.

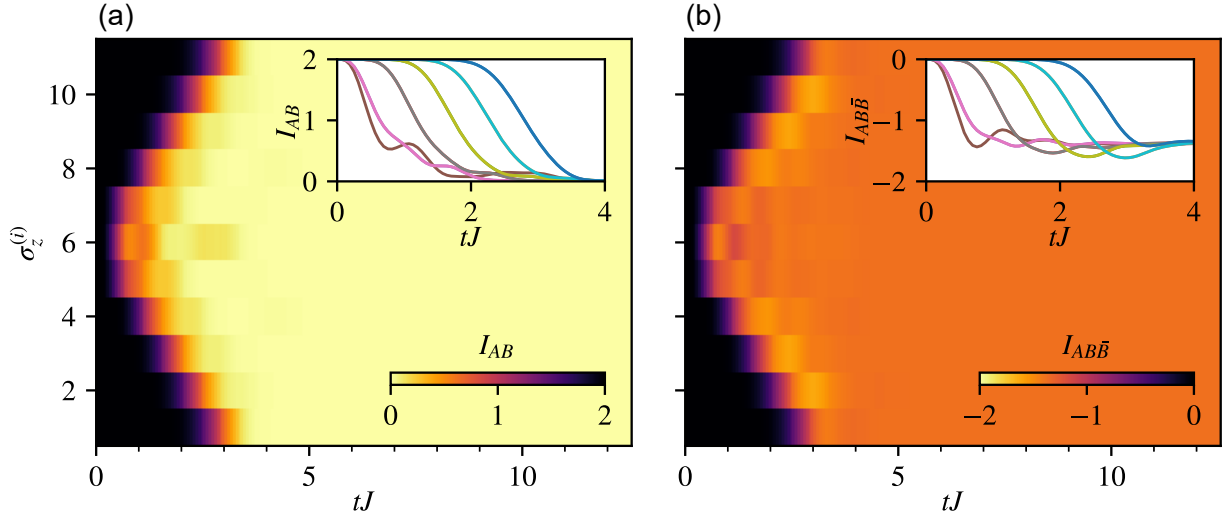


Figure 8: Time evolution of (a) BOMI and (b) TOMI for the local operator $\sigma_z^{(i)}$ at different sites in the chaotic chain model for the fully overlapping configuration. The y-axis corresponds to the location of the operator. Inset shows the same information with (a) BOMI and (b) TOMI on the y-axis. The subsystems, A and B , are centered at site 6 with size $l_A = l_B = 1$ and total size $L = 11$. The magnetic field is $(h_x, h_z) = (-1.05, 0.5)$.

3.2 Late-time evolution

Let us explain the late-time evolution of BOMI and TOMI in the spin chain (3.1).

Chaotic chain

Consider the chaotic phase of (3.1). The late-time evolution of the BOMI and TOMI of the local operators is independent of operators and boundary conditions, and is approximately equal to that of the BOMI and TOMI of the unitary operator. This is because the strong scrambling dynamics makes the state structureless. We have already seen in Figure 3 that the late-time value of the TOMI with size l is approximately equal to that with size $L - l$. The Page curve, a function of the sizes of in- and output (original and scattered) subsystems, effectively describes the late-time value of TOMI and BOMI.

Page curve

The Page curve is an effective description of the late-time value of OEE. The OEE of the local operator state in (2.20) for the original subspace A (scattered subsystem B) is proportional to the subsystem size ¹.

It is expected that if the dynamics has strong scrambling ability, then the late-time state is structureless. Therefore, the late-time OEE for a subsystem \mathcal{V} with total size \hat{L} is expected to be the entanglement entropy for the maximally entangled state:

$$S_{\mathcal{V}} = \begin{cases} \hat{L} & 0 \leq \hat{L} < L \\ L - \alpha & \hat{L} = L \\ 2L - \hat{L} & L < \hat{L} \leq 2L \end{cases}, \quad (3.3)$$

where \hat{L} is an even integer. The parameter α depends on the parameters h_x and h_z . If we

¹Here, OEE S_p is defined by

$$S_p = -\text{Tr}_p \rho_p \log_2 \rho_p.$$

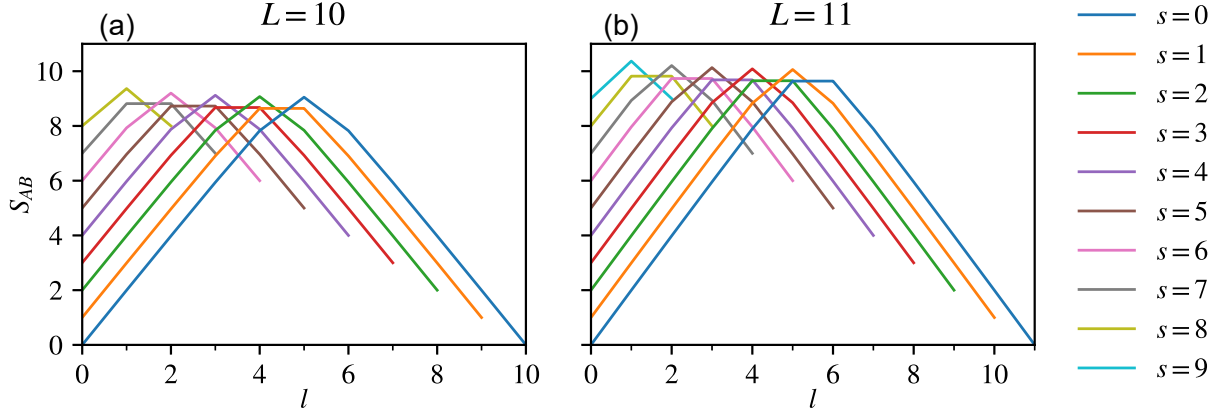


Figure 9: Late time entanglement entropy of the operator $U(t)$ in the chaotic chain model for the partially overlapping configuration (fully overlapping when $s = 0$). We show the entanglement entropy at time $t = 10^{12}$ for an (a) even system size $L = 10$ and (b) odd system size $L = 11$. The size of A is $l_A = l$ and B is $l_B = l + s$. The magnetic field is $(h_x, h_z) = (-1.05, 0.5)$. We show the entanglement entropy for periodic boundary conditions and operator $U(t)$ but note that the late time entanglement entropy is the same for open boundary conditions and operators $\sigma_x^{(i)}$, $\sigma_y^{(i)}$, and $\sigma_z^{(i)}$.

apply (3.3) to (2.22), we get the late time value:

$$I_{A,B} = \begin{cases} 0 & 0 \leq \hat{L} < L \\ \alpha & \hat{L} = L \\ 2(\hat{L} - L) & L < \hat{L} \leq 2L \end{cases}. \quad (3.4)$$

Since $I_{A,B}$ has to be non-negative, α must also be a non-negative number.

We plot the late-time value of $S_{A,B}$ for the full and partial overlap configurations in Figure 9, where $s = 0$ corresponds to the full overlap configuration. The behavior of $S_{A,B}$ in Figure 9 is consistent with (3.4) with $\hat{L} = 2l + s$. For the full overlap configuration, $\hat{L} = 2l$. Thus, when L is odd, we are not able to take $2l$ to be L . For the disjoint configuration, the size of $A \cup B$ is less than or equal to L since A and B are not overlapping. Therefore, $I_{A,B}$ should vanish at late time according to (3.3). However, in the numerical computation, that of $I_{A,B}$ does not vanish, but is a small value, β . Thus, β is not described by the Page curve.

We compute the late time value of $I_{A,B,\bar{B}}$ for the full overlap, partial overlap, and disjoint

configurations in terms of the Page curve. The late-time value of $I_{A,B,\bar{B}}$ in (a) of Figure 2 is

$$I_{A,B,\bar{B}} = \begin{cases} \alpha - 2l & 0 \leq 2l < L \\ 2\alpha - 2l & 2l = L \\ \alpha + 2(l - L) & L < 2l \leq 2L \end{cases}, \quad (3.5)$$

where L is an even integer, for simplicity. Consider the late-time value of $I_{A,B,\bar{B}}$ for the partial overlap configuration. In terms of the Page curve, the value is

$$I_{A,B,\bar{B}} = \begin{cases} -2l + \alpha & 0 \leq 2l < L, s = 0 \\ 2(\alpha - l) & L = 2l, s = 0 \\ 2(l - L) + \alpha & L < 2l \leq 2L, s = 0 \\ -2l & 0 \leq 2l + s < L, 0 < s \leq L \\ \alpha - 2l & 2l + s = L, 0 < s \leq L \\ 2(l - L + s) & L < 2l + s \leq 2L, 0 < s \leq L \end{cases}. \quad (3.6)$$

For the disjoint configuration, the late-time value of $I_{A,B,\bar{B}}$ computed in terms of Page curve is

$$I_{A,B\bar{B}} = \begin{cases} -2l_A & 0 < l_A < l_B \\ \alpha - 2l_A & 0 < l_A = l_B \\ -2l_B & 0 < l_B < l_A \leq L, \end{cases} \quad (3.7)$$

where l_A and l_B denotes the subsystem sizes of A and B .

Thermodynamic limit

Let us consider the late-time value of BOMI in the full overlap, partial overlap, and disjoint configurations, and TOMI in thermodynamic limit where we take L , the system size, to be infinite. By using (3.3) in the Page curve picture, the late-time value of BOMI in the full overlap, partial overlap, and disjoint configurations is equal to zero. Then, the late-time value of first and second terms of (2.23) is zero, whereas that of the last term is constant, so that the late-time value of TOMI is

$$I_{A,B,\bar{B}} \rightarrow -2l. \quad (3.8)$$

The late-time value of TOMI, $-2l$, is consistent with that of the TOMI of a unitary operator in 2 dimensional holographic CFT [21, 22, 23]. The late time values in (3.5), (3.6), (3.7) and

(3.8) show that finite size effects prevent the dynamics from delocalizing quantum information since the late time value of TOMI in an infinite space is smaller in magnitude compared to a finite space.

4 Time evolution of BOMI and TOMI in a disordered spin chain

Let us study the time evolution of the BOMI and TOMI of $U(t)$, $\sigma_x^{(i)}$, $\sigma_y^{(i)}$, and $\sigma_z^{(i)}$ in a spin system with disorder:

$$H_{\text{MBL}} = \sum_{i=1}^L J \vec{\sigma}^{(i)} \cdot \vec{\sigma}^{(i+1)} + \sum_{i=1}^L h_i \sigma_z^{(i)}, \quad (4.1)$$

where $\vec{\sigma}^{(i)}$ is the vector of Pauli spin operators and h_i is a disorder parameter drawn from a uniform random distribution, $h_i \in [-w, w]$. In Figure 10, 11, and 12, we show the time evolution of BOMI and TOMI in the full overlap, partial overlap, and disjoint configurations, respectively.

Let us explain the time evolution of BOMI and TOMI in the small and large w regions and near critical point.

- **small w region ($w = 1$):** As in [61, 62, 63, 64, 33], (4.1) with small $w \ll 4$ is in the chaotic phase. Therefore, the late-time value of BOMI and TOMI is independent of operators and boundary conditions, and is well-described in terms of the Page curve (See, Figures 10, 11, and 12).
- **near critical region ($w = 3$):** The time evolution of BOMI and TOMI depends on the operators and boundary conditions. In the full and partial overlap configurations, the late time value of BOMI and TOMI is larger than that in (4.1) with $w = 1$. In the disjoint configuration, the late time value of BOMI and TOMI in the chaotic phase ($w = 1$) is independent of the distance between two intervals, d , but that of BOMI and TOMI near the critical point ($w = 3$) depends on d . In (4.1) with OBC, the late time value of BOMI is a monotonically decreasing function of d , but that of TOMI

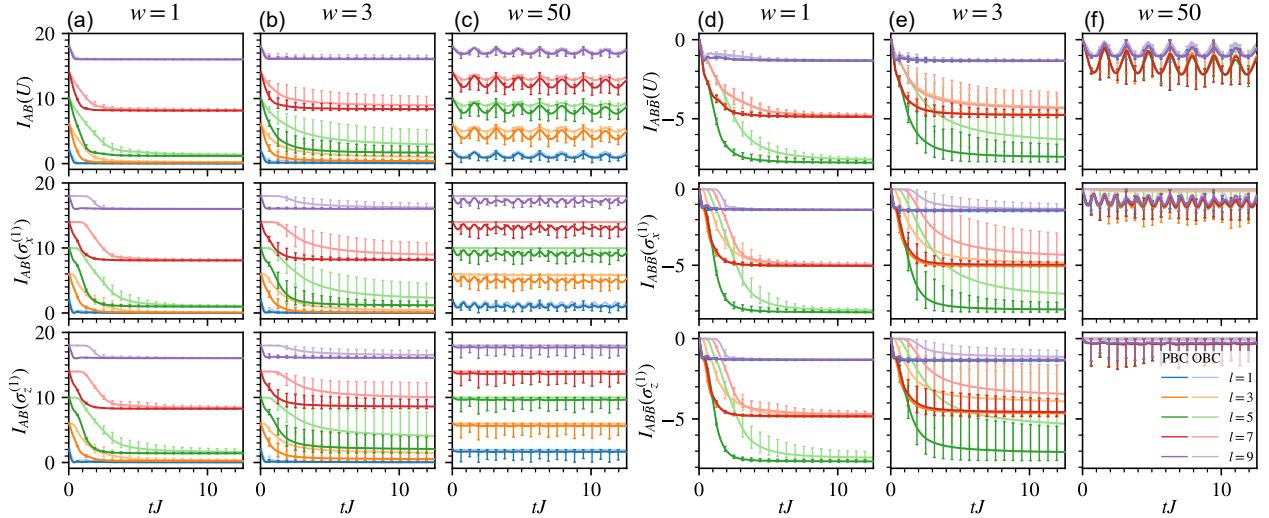


Figure 10: Time evolution of (a-c) BOMI and (d-f) TOMI of the operators $U(t)$, $\sigma_x^{(1)}$, $\sigma_y^{(1)}$, and $\sigma_z^{(1)}$ in the disordered spin chain model for the fully overlapping configuration. The local operators are located at the left boundary of A and B and the size of A and B are equal, $l_A = l_B = l$. The disorder strength is (a,d) $w = 1$, (b,e) $w = 3$, and (c,f) $w = 50$. Solid lines show the mean over 20 disorder configurations and error bars show the min and max. Dark lines correspond to periodic boundary conditions and light lines correspond to open boundary conditions. The total number of sites is $L = 10$.

is a monotonically increasing function of d . The d -dependence of BOMI shows MBL prevents the information from spreading, and that of TOMI shows MBL prevents the information from being delocalized.

- **large w region ($w = 50$):** In the large w region ($w = 50$), BOMI and TOMI of $\sigma_z(t)$ are almost time-independent. This is because $\sigma_z^{(i)}(t)$ is well approximated by

$$\sigma_z^{(i)}(t) \approx e^{iH_{\text{eff}}}\sigma_z^{(i)}e^{-iH_{\text{eff}}} = \sigma_z^{(i)}, \quad (4.2)$$

where H_{eff} is described in the next section.

As in Figures 10 and 11, for the full and partial overlap configurations, the value of BOMI and TOMI with $w > w_{\text{cri}}$ increases, when w increases. As in Figure 12, when w increases, the value of the BOMI with $w > w_{\text{cri}}$ in the disjoint configuration decreases, but the value of the TOMI decreases. The BOMI and TOMI in some configurations are oscillating function of t . Let us explain why they oscillate in terms of an effective

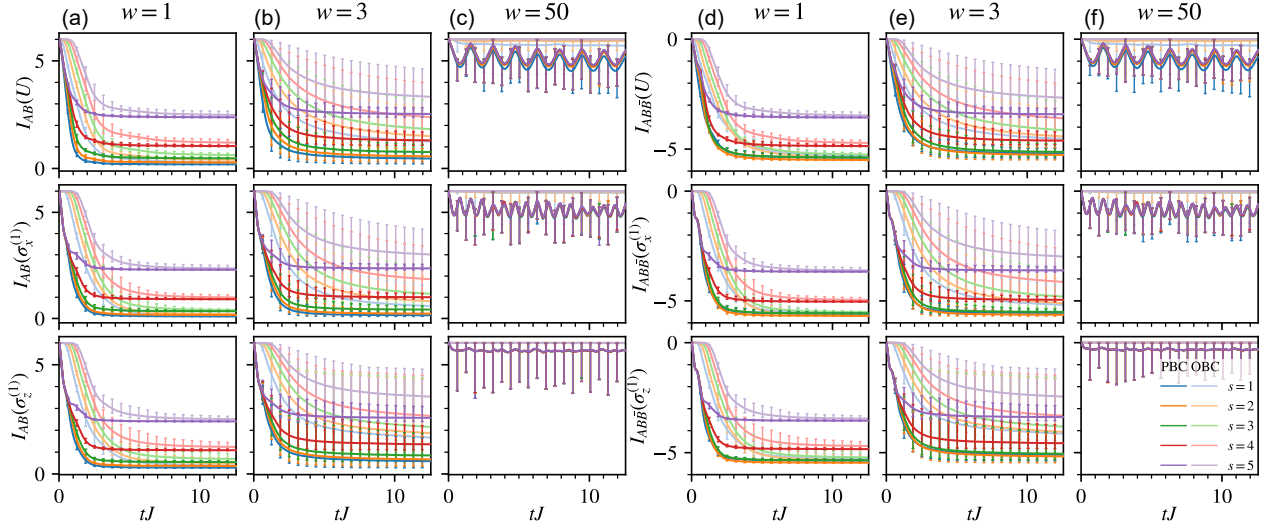


Figure 11: Time evolution of (a-c) BOMI and (d-f) TOMI of the operators U , $\sigma_x^{(1)}$, $\sigma_y^{(1)}$, and $\sigma_z^{(1)}$ in the disordered spin chain model for the partially overlapping configuration. The local operators are located at the left boundary of A and B and the size of B is greater than the size of A by s , $l_A + s = l_B$. The disorder strength is (a,d) $w = 1$, (b,e) $w = 3$, and (c,f) $w = 50$. Solid lines show the mean over 20 disorder configurations and error bars show the min and max. Dark lines correspond to periodic boundary conditions and light lines correspond to open boundary conditions. The total number of sites is $L = 10$ and the number of sites in A is $l_A = 3$.

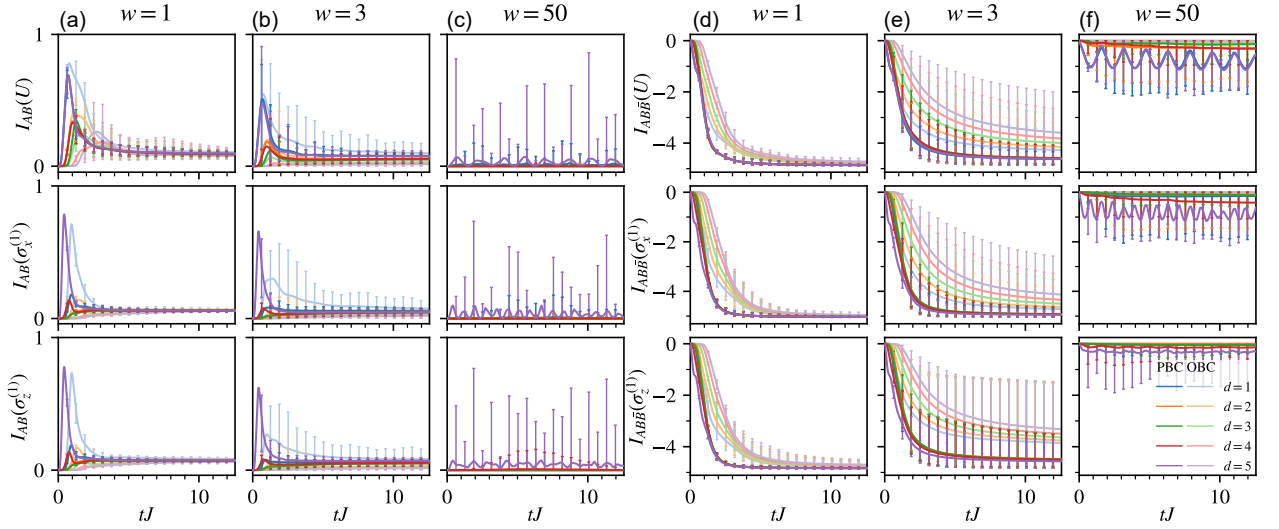


Figure 12: Time evolution of (a-c) BOMI and (d-f) TOMI of the operators U , $\sigma_x^{(1)}$, $\sigma_y^{(1)}$, and $\sigma_z^{(1)}$ in the disordered spin chain model for the disjoint configuration. The local operators are located at the left boundary of A and the left boundary of B is a distance d from the right boundary of A . The disorder strength is (a,d) $w = 1$, (b,e) $w = 3$, and (c,f) $w = 50$. Solid lines show the mean over 20 disorder configurations and error bars show the min and max. Dark lines correspond to periodic boundary conditions and light lines correspond to open boundary conditions. The total number of sites is $L = 10$ and the number of sites in A and B are $l_A = l_B = 3$.

hamiltonian in the next subsection.

4.1 Effective theory in the strong disordered phase.

Consider the limit $J \ll w$ with OBC for simplicity. The energies of (4.1) to first order in J/w are

$$E \approx J \sum_{i=1}^{L-1} \sigma_z^{(i)} \sigma_z^{(i+1)} + \sum_{i=1}^L h_i \sigma_z^{(i)} \quad (4.3)$$

which are the same energies as the disordered Ising chain. We consider the effective Hamiltonian

$$H_{\text{eff}} = J \sum_{i=1}^{L-1} \sigma_z^{(i)} \sigma_z^{(i+1)} + \sum_{i=1}^L h_i \sigma_z^{(i)} \quad (4.4)$$

The effective Hamiltonian is diagonal in the $\sigma_z^{(i)}$ basis and the entanglement entropy is exactly solvable. To demonstrate this, consider the local operator $\sigma_x^{(1)}$. The operator in the eigenbasis of H_{eff} is given by

$$\begin{aligned} \sigma_x^{(1)} &= \sum_{\{\sigma_z, \tau_z\}} |\sigma_z^{(1)} \dots \sigma_z^{(L)}\rangle e^{itH_{\text{eff}}[\{\sigma_z\}]} \langle \sigma_z^{(1)} \dots \sigma_z^{(L)} | \sigma_x^{(1)} | \tau_z^{(1)} \dots \tau_z^{(L)} \rangle e^{-itH_{\text{eff}}[\{\tau_z\}]} \langle \tau_z^{(1)} \dots \tau_z^{(L)} | \\ &= \sum_{\{\sigma_z\}} |\sigma_z^{(1)} \dots \sigma_z^{(L)}\rangle \exp \{ 2it [J \sigma_z^{(1)} \sigma_z^{(2)} + h_1 \sigma_z^{(1)}] \} \langle \bar{\sigma}_z^{(1)} \dots \sigma_z^{(L)} | \end{aligned}$$

where the bar denotes flipping the spin. The density matrix for the dual state to $\sigma_x^{(1)}$ is given by

$$\begin{aligned} \rho &= \frac{1}{2^L} \sum_{\{\sigma_z, \tau_z\}} \exp \{ 2it [J (\sigma_z^{(1)} \sigma_z^{(2)} - \tau_z^{(1)} \tau_z^{(2)}) + h_1 (\sigma_z^{(1)} - \tau_z^{(1)})] \} \\ &\quad \times |\sigma_z^{(1)} \dots \sigma_z^{(L)}\rangle \langle \tau_z^{(1)} \dots \tau_z^{(L)} |_{\text{in}} \otimes |\bar{\sigma}_z^{(1)} \dots \sigma_z^{(L)}\rangle \langle \bar{\tau}_z^{(1)} \dots \tau_z^{(L)} |_{\text{out}} \end{aligned}$$

We see that if both $\sigma_z^{(1)}$ and $\sigma_z^{(2)}$ are traced out in either the input or output space, then the exponential becomes unity and the density matrix becomes constant in time. If we trace out either $\sigma_z^{(1)}$ or $\sigma_z^{(2)}$, then we get a cosine dependence on time. As an example, we show the mutual information when A and B are the original and scattered spaces that only includes site 1, $A = \mathcal{H}_{1_{\text{in}}}$ and $B = \mathcal{H}_{1_{\text{out}}}$. For subsystems that are not overlapping in the input and

output spaces, we trace out both $\sigma_z^{(1)}$ and $\sigma_z^{(2)}$ and the exponential becomes unity. Thus, the reduced density matrix and entanglement entropy is given by

$$\begin{aligned}
\rho_A &= \frac{1}{2} \mathbb{1}_{\mathcal{H}_A} & \rho_B &= \frac{1}{2} \mathbb{1}_{\mathcal{H}_B} & \rho_{\bar{A}} &= \frac{1}{2^{L-1}} \mathbb{1}_{\mathcal{H}_{\bar{A}}} \\
\rho_{\bar{B}} &= \frac{1}{2^{L-1}} \mathbb{1}_{\mathcal{H}_{\bar{B}}} & \rho_{A\cup\bar{B}} &= \frac{1}{2^L} \mathbb{1}_{\mathcal{H}_A} \otimes \mathbb{1}_{\mathcal{H}_{\bar{B}}} & \rho_{B\cup\bar{B}} &= \frac{1}{2^L} \mathbb{1}_{\mathcal{H}_B} \otimes \mathbb{1}_{\mathcal{H}_{\bar{B}}} \\
S_A &= \log(2) & S_B &= \log(2) & S_{\bar{A}} &= (L-1) \log(2) \\
S_{\bar{B}} &= (L-1) \log(2) & S_{A\cup\bar{B}} &= L \log(2) & S_{B\cup\bar{B}} &= L \log(2)
\end{aligned}$$

For the overlap, the reduced density matrix and entanglement entropy are given by

$$\begin{aligned}
\rho_{A\cup B} &= \frac{1}{2} \sum_{\sigma_z^{(1)}, \tau_z^{(1)}} \cos(2tJ(\sigma_z^{(1)} - \tau_z^{(1)})) \exp[2it h_1(\sigma_z^{(1)} - \tau_z^{(1)})] |\sigma_z^{(1)}\rangle \langle \tau_z^{(1)}|_{\text{in}} \otimes |\bar{\sigma}_z^{(1)}\rangle \langle \bar{\tau}_z^{(1)}|_{\text{out}} \\
S_{A\cup B} &= -\cos^2(2tJ) \log(\cos^2(2tJ)) - \sin^2(2tJ) \log(\sin^2(2tJ))
\end{aligned}$$

Therefore,

$$I_{A,B} = 2 \log(2) - S_{A\cup B} \quad I_{A,\bar{B}} = 0 \quad I_{A,B,\bar{B}} = -S_{A\cup B}$$

In Figure 13, we show the time evolution of BOMI and TOMI for various disorder strengths. The BOMI and TOMI are well described by the effective Hamiltonian for $w/J > 10^2$. In strong disorder region, the oscillation of BOMI and TOMI depends on only the local interaction J , even though the reduced density matrix depends on not only J , but also the disorder, h_i . We can follow a similar procedure to get the density matrix for different operators.

$$\begin{aligned}
\rho(\sigma_z^{(i)}) &= \frac{1}{2^L} \sum_{\{\sigma_z, \tau_z\}} \sigma_z^{(i)} |\sigma_z^{(1)} \dots \sigma_z^{(L)}\rangle \langle \tau_z^{(1)} \dots \tau_z^{(L)}|_{\text{in}} \otimes |\sigma_z^{(1)} \dots \sigma_z^{(L)}\rangle \langle \tau_z^{(1)} \dots \tau_z^{(L)}|_{\text{out}} \\
\rho(U) &= \frac{1}{2^L} \sum_{\{\sigma_z, \tau_z\}} e^{-it(H_{\text{eff}}[\{\sigma_z\}] - H_{\text{eff}}[\{\tau_z\}])} |\sigma_z^{(1)} \dots \sigma_z^{(L)}\rangle \langle \tau_z^{(1)} \dots \tau_z^{(L)}|_{\text{in}} \otimes |\sigma_z^{(1)} \dots \sigma_z^{(L)}\rangle \langle \tau_z^{(1)} \dots \tau_z^{(L)}|_{\text{out}}
\end{aligned}$$

$\sigma_x^{(1)}$ and $\sigma_y^{(1)}$ are related by a rotational symmetry of the spins around the \hat{z} axis. The density matrix for the $\sigma_z^{(i)}$ operators do not have any time dependence and any BOMI or TOMI will be constant. For the time-evolution operator, we see that if all the σ_z and τ_z are the same, then the BOMI and TOMI will be constant. Therefore, we only see oscillations for the fully overlapping and partially overlapping cases.

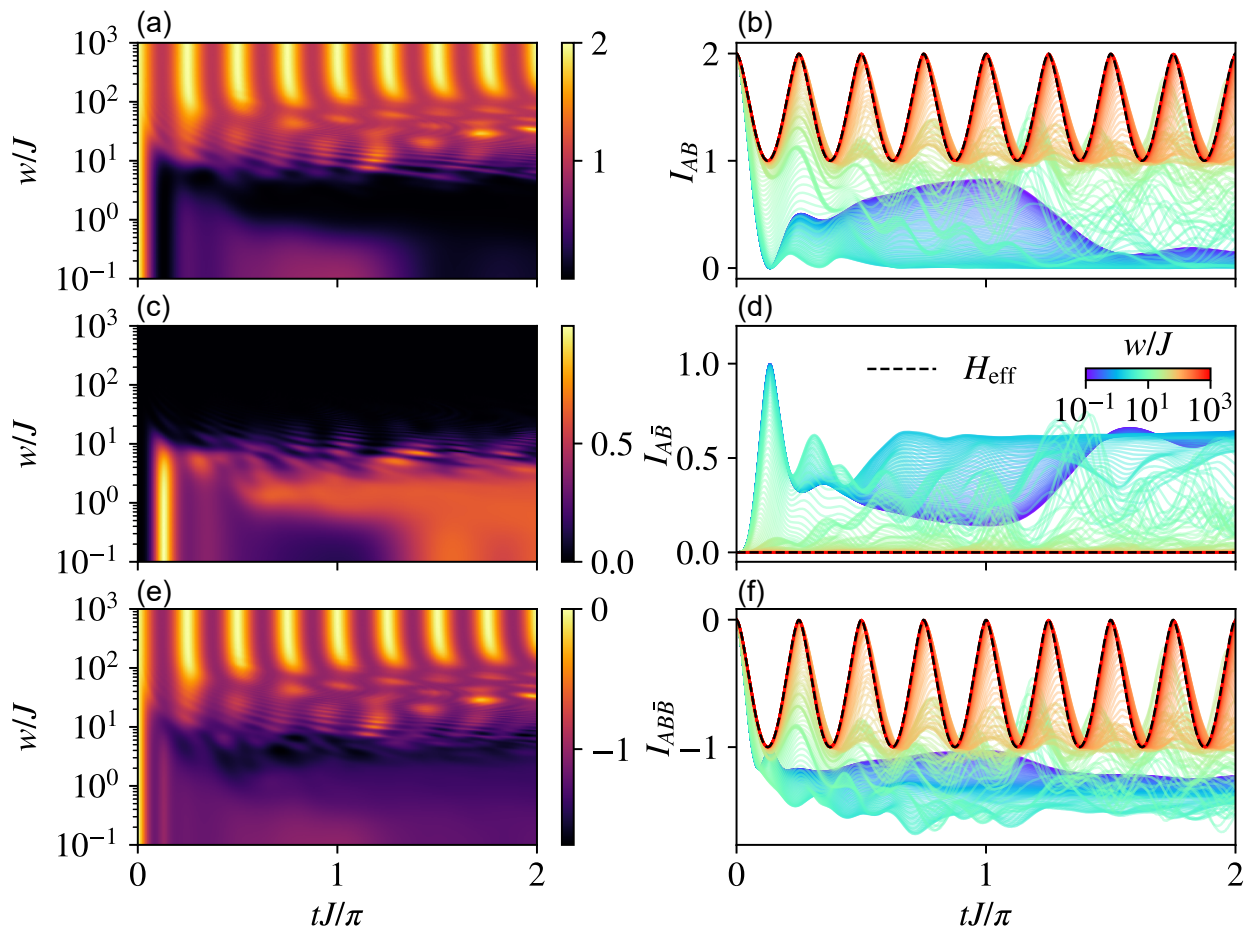


Figure 13: Time evolution vs. disorder strength of (a-d) BOMI and (e-f) TOMI of the operator $\sigma_x^{(1)}$ in the disordered spin chain model for the fully overlapping configuration. We use a single disorder configuration to show the evolution over varying disorder strengths. Dashed lines in (b,d,f) show the BOMI and TOMI using the effective Hamiltonian, corresponding to the $J \ll w$ regime of the disordered spin chain. The subsystems, A and B , are centered at site 1 with size $l_A = l_B = 1$ and total size $L = 10$ using open boundary conditions.

5 Discussions and Future directions

Discussions

Let us summarize the results, compare with the CFT results [21, 22, 23], and comment on a few future directions.

Summary

We have studied the time evolution of BOMI and TOMI for the unitary time evolution operator and Pauli's spin operators in the chaotic chain (3.1) and MBL chain (4.1).

We found that:

- **Chaotic chain:** The early-time evolution of TOMI and BOMI is qualitatively described in terms of an effective light cone picture. Their late-time evolution is independent of the boundary condition and operators, and their late-time value is quantitatively explained by the Page curve. For PBC, quantum revival does not occur and the compactness of space time prevents the dynamics from delocalizing the quantum information.
- **Disordered spin chain:** In the weak disordered system ($w = 1$), the late-time value of BOMI and TOMI is well-described by the Page curve. In the strong disordered system ($w > w_{\text{cri}}$), BOMI and TOMI in full and partial overlap configurations increases when w increases. However, for the disjoint configuration, when w increases, BOMI decreases and TOMI increases. This is because MBL prevents the information from propagating and delocalizing. In the very strong disorder system ($w = 50$), BOMI and TOMI in some of configurations oscillate with respect to time. This oscillation is well-described by the effective Hamiltonian.

Comparison with CFTs

Here, we compare the late time value of BOMI and TOMI derived by the Page curve with that of holographic CFTs [21, 22, 23], which are theories that have a gravity dual. After

taking the thermodynamic limit, the Page curve describes the late time value of BOMI. As in (3.8), when we take the thermodynamic limit, the late-time value of TOMI in the chaotic phase of (3.1) is ²

$$I(A, B, \bar{B}) = -2l \cdot \log 2, \quad (5.1)$$

where 2 counts the dimension of the local Hilbert space. In the holographic CFT, the late-time value of TOMI is

$$I_{A,B,\bar{B}} = -2l \log \left[e^{\left(\frac{\pi c}{6\epsilon}\right)} \right], \quad (5.2)$$

where c is the central charge, and ϵ is the scale which characterizes the initial state, $|\Psi\rangle_{\text{initial}} \propto \sum_a \frac{1}{\epsilon} C_a e^{-itE_a} |a\rangle$. Therefore, we expect the chaotic chain with approximately $e^{\left(\frac{\pi c}{6\epsilon}\right)}$ local degrees of freedom to mimic the dynamical properties of holographic CFT.

Future directions

Let us comment on a few future directions:

- 1 An important future direction is to construct a tractable system with a large number of local degrees of freedom and strong scrambling ability in order to mimic holographic CFTs.
- 2 To compute logarithmic negativity and reflected entropy is also interesting. In holographic CFTs, these values show phase transition-like behavior [20, 21, 22, 23]. It would be interesting to see whether logarithmic negativity or reflected entropy in the chaotic chain also show such a behavior.
- 3 We numerically found that the late time value of TOMI in the chaotic chain on the compact manifold was non-vanishing. It would be interesting to analytically compute this in a 2 dimensional holographic CFT on a compact manifold to find the finite size correction compared to a non-compact holographic CFT.

²Except for Section 5, BOMI and TOMI are divided by $\log 2$

Acknowledgments

We would like to thank Shinsei Ryu, Jonah Kunder-Flam, and Mao Tian Tan for useful discussions. The work of M.T. was partially supported by Grant-in-Aid No. JP17K17822, No. JP20H05270 and No. JP20K03787 from JSPS of Japan. The work of M.N. was partially supported by Grant-in-Aid No. JP19K14724 from JSPS of Japan. M.N. and M.T. thank the Yukawa Institute for Theoretical Physics at Kyoto University for hospitality during the workshops YITP-T-18-04 "New Frontiers in String Theory 2018" and YITP-T-19-03 "Quantum Information and String Theory 2019".

References

- [1] M. Srednicki, "Chaos and quantum thermalization," *Phys. Rev. E*, vol. 50, pp. 888–901, Aug 1994.
- [2] J. M. Deutsch, "Quantum statistical mechanics in a closed system," *Phys. Rev. A*, vol. 43, pp. 2046–2049, Feb 1991.
- [3] M. Rigol, V. Dunjko, and M. Olshanii, "Thermalization and its mechanism for generic isolated quantum systems," *Nature*, vol. 452, pp. 854–858, Apr 2008.
- [4] J. Maldacena, "The Large-N Limit of Superconformal Field Theories and Supergravity," *International Journal of Theoretical Physics*, vol. 38, pp. 1113–1133, Jan 1999.
- [5] S. Ryu and T. Takayanagi, "Holographic Derivation of Entanglement Entropy from the anti de Sitter Space/Conformal Field Theory Correspondence," *Phys. Rev. Lett.*, vol. 96, p. 181602, May 2006.
- [6] S. Ryu and T. Takayanagi, "Aspects of holographic entanglement entropy," *Journal of High Energy Physics*, vol. 8, p. 045, Aug. 2006.

- [7] P. Calabrese and J. Cardy, “Evolution of entanglement entropy in one-dimensional systems,” *Journal of Statistical Mechanics: Theory and Experiment*, vol. 4, p. 04010, Apr. 2005.
- [8] J. Abajo-Arrastia, J. Aparício, and E. López, “Holographic evolution of entanglement entropy,” *Journal of High Energy Physics*, vol. 2010, p. 149, Nov 2010.
- [9] T. Hartman and J. Maldacena, “Time evolution of entanglement entropy from black hole interiors,” *Journal of High Energy Physics*, vol. 5, p. 14, May 2013.
- [10] H. Liu and S. J. Suh, “Entanglement Tsunami: Universal Scaling in Holographic Thermalization,” *Phys. Rev. Lett.*, vol. 112, p. 011601, Jan 2014.
- [11] C. T. Asplund and A. Bernamonti, “Mutual information after a local quench in conformal field theory,” *Phys. Rev. D*, vol. 89, p. 066015, Mar 2014.
- [12] C. T. Asplund, A. Bernamonti, F. Galli, and T. Hartman, “Entanglement scrambling in 2d conformal field theory,” *Journal of High Energy Physics*, vol. 9, p. 110, Sept. 2015.
- [13] P. Hayden, M. Headrick, and A. Maloney, “Holographic mutual information is monogamous,” *Phys. Rev. D*, vol. 87, p. 046003, Feb 2013.
- [14] P. Hosur, X.-L. Qi, D. A. Roberts, and B. Yoshida, “Chaos in quantum channels,” *Journal of High Energy Physics*, vol. 2016, p. 4, Feb 2016.
- [15] T. Zhou and D. J. Luitz, “Operator entanglement entropy of the time evolution operator in chaotic systems,” *Phys. Rev. B*, vol. 95, p. 094206, Mar. 2017.
- [16] V. Alba, J. Dubail, and M. Medenjak, “Operator Entanglement in Interacting Integrable Quantum Systems: The Case of the Rule 54 Chain,” *Physical Review Letters*, vol. 122, p. 250603, Jun 2019.

- [17] C. W. von Keyserlingk, T. Rakovszky, F. Pollmann, and S. L. Sondhi, “Operator Hydrodynamics, OTOCs, and Entanglement Growth in Systems without Conservation Laws,” *Physical Review X*, vol. 8, p. 021013, Apr. 2018.
- [18] A. Nahum, J. Ruhman, S. Vijay, and J. Haah, “Quantum Entanglement Growth under Random Unitary Dynamics,” *Physical Review X*, vol. 7, p. 031016, July 2017.
- [19] C. Jonay, D. A. Huse, and A. Nahum, “Coarse-grained dynamics of operator and state entanglement,” *ArXiv e-prints 1803.00089*, Feb. 2018.
- [20] J. Kudler-Flam, L. Nie, and S. Ryu, “Conformal field theory and the web of quantum chaos diagnostics,” *arXiv e-prints*, p. arXiv:1910.14575, Oct 2019.
- [21] L. Nie, M. Nozaki, S. Ryu, and M. Tian Tan, “Signature of quantum chaos in operator entanglement in 2d CFTs,” *arXiv e-prints*, p. arXiv:1812.00013, Nov 2018.
- [22] J. Kudler-Flam, M. Nozaki, S. Ryu, and M. Tian Tan, “Quantum vs. classical information: operator negativity as a probe of scrambling,” *arXiv e-prints*, p. arXiv:1906.07639, Jun 2019.
- [23] J. Kudler-Flam, M. Nozaki, S. Ryu, and M. Tian Tan, “Entanglement of Local Operators and the Butterfly Effect,” *arXiv e-prints*, p. arXiv:2005.14243, May 2020.
- [24] I. MacCormack, M. Tian Tan, J. Kudler-Flam, and S. Ryu, “Operator and entanglement growth in non-thermalizing systems: many-body localization and the random singlet phase,” *arXiv e-prints*, p. arXiv:2001.08222, Jan. 2020.
- [25] D. N. Page, “Average entropy of a subsystem,” *Physical Review Letters*, vol. 71, pp. 1291–1294, Aug 1993.
- [26] S. Sen, “Average entropy of a quantum subsystem,” *Physical Review Letters*, vol. 77, pp. 1–3, Jul 1996.

- [27] P. Calabrese and J. Cardy, “Quantum quenches in 1 + 1 dimensional conformal field theories,” *Journal of Statistical Mechanics: Theory and Experiment*, vol. 6, p. 064003, Jun 2016.
- [28] J. Cardy, “Thermalization and Revivals after a Quantum Quench in Conformal Field Theory,” *Phys. Rev. Lett.*, vol. 112, p. 220401, Jun 2014.
- [29] M. C. Bañuls, J. I. Cirac, and M. B. Hastings, “Strong and Weak Thermalization of Infinite Nonintegrable Quantum Systems,” *Phys. Rev. Lett.*, vol. 106, p. 050405, Feb 2011.
- [30] D. A. Roberts, D. Stanford, and L. Susskind, “Localized shocks,” *Journal of High Energy Physics*, vol. 2015, p. 51, Mar 2015.
- [31] D. A. Roberts, D. Stanford, and A. Streicher, “Operator growth in the SYK model,” *Journal of High Energy Physics*, vol. 2018, p. 122, Jun 2018.
- [32] X.-L. Qi, E. J. Davis, A. Periwai, and M. Schleier-Smith, “Measuring operator size growth in quantum quench experiments,” *arXiv e-prints*, p. arXiv:1906.00524, Jun 2019.
- [33] F. Alet and N. Laflorencie, “Many-body localization: An introduction and selected topics,” *Comptes Rendus Physique*, vol. 19, no. 6, pp. 498 – 525, 2018. Quantum simulation / Simulation quantique.
- [34] S. A. Parameswaran and R. Vasseur, “Many-body localization, symmetry and topology,” *Reports on Progress in Physics*, vol. 81, p. 082501, Jul 2018.
- [35] D. A. Abanin, E. Altman, I. Bloch, and M. Serbyn, “Colloquium: Many-body localization, thermalization, and entanglement,” *Rev. Mod. Phys.*, vol. 91, p. 021001, May 2019.
- [36] P. W. Anderson, “Absence of diffusion in certain random lattices,” *Phys. Rev.*, vol. 109, pp. 1492–1505, Mar 1958.

- [37] L. Fleishman and P. W. Anderson, “Interactions and the anderson transition,” *Phys. Rev. B*, vol. 21, pp. 2366–2377, Mar 1980.
- [38] A. M. Finkel’shtein, “Influence of coulomb interaction on the properties of disordered metals,” *J. Exp. Theor. Phys.*, vol. 57, p. 97, Jan 1983.
- [39] T. Giamarchi and H. J. Schulz, “Anderson localization and interactions in one-dimensional metals,” *Phys. Rev. B*, vol. 37, pp. 325–340, Jan 1988.
- [40] B. L. Altshuler, Y. Gefen, A. Kamenev, and L. S. Levitov, “Quasiparticle lifetime in a finite system: A nonperturbative approach,” *Phys. Rev. Lett.*, vol. 78, pp. 2803–2806, Apr 1997.
- [41] I. V. Gornyi, A. D. Mirlin, and D. G. Polyakov, “Interacting electrons in disordered wires: Anderson localization and low- t transport,” *Phys. Rev. Lett.*, vol. 95, p. 206603, Nov 2005.
- [42] D. Basko, I. Aleiner, and B. Altshuler, “Metal–insulator transition in a weakly interacting many-electron system with localized single-particle states,” *Annals of Physics*, vol. 321, no. 5, pp. 1126 – 1205, 2006.
- [43] Z. Papić, E. M. Stoudenmire, and D. A. Abanin, “Many-body localization in disorder-free systems: The importance of finite-size constraints,” *Annals of Physics*, vol. 362, pp. 714 – 725, 2015.
- [44] J. M. Deutsch, “Quantum statistical mechanics in a closed system,” *Phys. Rev. A*, vol. 43, pp. 2046–2049, Feb 1991.
- [45] M. Srednicki, “Chaos and quantum thermalization,” *Phys. Rev. E*, vol. 50, pp. 888–901, Aug 1994.

- [46] O. Bohigas, M. J. Giannoni, and C. Schmit, “Characterization of chaotic quantum spectra and universality of level fluctuation laws,” *Phys. Rev. Lett.*, vol. 52, pp. 1–4, Jan 1984.
- [47] H. Kim and D. A. Huse, “Ballistic spreading of entanglement in a diffusive nonintegrable system,” *Phys. Rev. Lett.*, vol. 111, p. 127205, Sep 2013.
- [48] M. Žnidarič, T. c. v. Prosen, and P. Prelovšek, “Many-body localization in the heisenberg xxz magnet in a random field,” *Phys. Rev. B*, vol. 77, p. 064426, Feb 2008.
- [49] J. H. Bardarson, F. Pollmann, and J. E. Moore, “Unbounded growth of entanglement in models of many-body localization,” *Phys. Rev. Lett.*, vol. 109, p. 017202, Jul 2012.
- [50] M. Serbyn, Z. Papić, and D. A. Abanin, “Universal slow growth of entanglement in interacting strongly disordered systems,” *Phys. Rev. Lett.*, vol. 110, p. 260601, Jun 2013.
- [51] D. A. Huse, R. Nandkishore, and V. Oganesyan, “Phenomenology of fully many-body-localized systems,” *Phys. Rev. B*, vol. 90, p. 174202, Nov 2014.
- [52] B. Bauer and C. Nayak, “Area laws in a many-body localized state and its implications for topological order,” *Journal of Statistical Mechanics: Theory and Experiment*, vol. 2013, p. P09005, Sep 2013.
- [53] M. Schreiber, S. S. Hodgman, P. Bordia, H. P. Lüschen, M. H. Fischer, R. Vosk, E. Altman, U. Schneider, and I. Bloch, “Observation of many-body localization of interacting fermions in a quasirandom optical lattice,” *Science*, vol. 349, no. 6250, pp. 842–845, 2015.
- [54] J.-y. Choi, S. Hild, J. Zeiher, P. Schauß, A. Rubio-Abadal, T. Yefsah, V. Khemani, D. A. Huse, I. Bloch, and C. Gross, “Exploring the many-body localization transition in two dimensions,” *Science*, vol. 352, no. 6293, pp. 1547–1552, 2016.

- [55] P. Bordia, H. P. Lüschen, S. S. Hodgman, M. Schreiber, I. Bloch, and U. Schneider, “Coupling identical one-dimensional many-body localized systems,” *Phys. Rev. Lett.*, vol. 116, p. 140401, Apr 2016.
- [56] A. Lukin, M. Rispoli, R. Schittko, M. E. Tai, A. M. Kaufman, S. Choi, V. Khemani, J. Léonard, and M. Greiner, “Probing entanglement in a many-body-localized system,” *Science*, vol. 364, no. 6437, pp. 256–260, 2019.
- [57] J. Smith, A. Lee, P. Richerme, B. Neyenhuis, P. W. Hess, P. Hauke, M. Heyl, D. A. Huse, and C. Monroe, “Many-body localization in a quantum simulator with programmable random disorder,” *Nature Physics*, vol. 12, no. 10, pp. 907–911, 2016.
- [58] S. H. Shenker and D. Stanford, “Black holes and the butterfly effect,” *Journal of High Energy Physics*, vol. 3, p. 67, Mar. 2014.
- [59] P. Pfeuty, “The one-dimensional ising model with a transverse field,” *ANNALS of Physics*, vol. 57, no. 1, pp. 79–90, 1970.
- [60] A. Coser, E. Tonni, and P. Calabrese, “Entanglement negativity after a global quantum quench,” *Journal of Statistical Mechanics: Theory and Experiment*, vol. 2014, p. 12017, Dec. 2014.
- [61] D. J. Luitz, N. Laflorencie, and F. Alet, “Many-body localization edge in the random-field heisenberg chain,” *Phys. Rev. B*, vol. 91, p. 081103, Feb 2015.
- [62] T. Devakul and R. R. P. Singh, “Early breakdown of area-law entanglement at the many-body delocalization transition,” *Phys. Rev. Lett.*, vol. 115, p. 187201, Oct 2015.
- [63] S. P. Lim and D. N. Sheng, “Many-body localization and transition by density matrix renormalization group and exact diagonalization studies,” *Phys. Rev. B*, vol. 94, p. 045111, Jul 2016.

- [64] V. Khemani, S. P. Lim, D. N. Sheng, and D. A. Huse, “Critical properties of the many-body localization transition,” *Phys. Rev. X*, vol. 7, p. 021013, Apr 2017.